Progress In Electromagnetics Research, Vol. 110, 103–124, 2010

COMPARATIVE STUDY OF RMA AND PFA ON THEIR RESPONSES TO MOVING TARGET

X. H. Mao, D. Y. Zhu, L. Ding, and Z. D. Zhu

Department of Electronic Engineering
Nanjing University of Aeronautics and Astronautics
Nanjing 210016, China

Abstract—The synthetic aperture radar (SAR) signatures of moving target are the basis of ground moving target indication and imaging (GMTI&Im) in the framework of SAR systems. However, previous studies are mainly based on the 2-D separable SAR processing, and little work has been done to investigate the signatures of moving target after the application of a particular fine resolution SAR image formation algorithm. In this paper, we derive the image spectrum of moving target after two representative fine resolution SAR image formation algorithms, i.e., the range migration algorithm (RMA) and polar format algorithm (PFA), respectively. Based on the spectrum derived, detailed analysis on the SAR signatures of moving target, including the geometric displacement, residual range migration, and defocusing effect in both the range and azimuth dimensions are performed. The presented work might be helpful when considering a SAR system with the capability of ground moving target indication and imaging (GMTI&Im).

1. INTRODUCTION

Synthetic aperture radar (SAR) is a coherent imaging system capable of generating fine resolution images of stationary targets on the ground, which has become an important tool in military intelligence, surveillance, and reconnaissance [1–7]. With the development of SAR technology, more specialized radar problems are being studied in the framework of SAR systems. A prominent example is ground moving target indication and imaging (GMTI&Im) in a SAR scene [8–13]. As well known when a conventional SAR processing algorithm is applied

Received 6 September 2010, Accepted 25 October 2010, Scheduled 11 November 2010
Corresponding author: Xinhua Mao (xinhua@nuaa.edu.cn).

to a scene containing moving targets, the images of moving targets are typically dislocated and smeared out due to the additional phase error and range migration induced by the motion. Therefore, a prediction of the response of the SAR processing algorithm employed to the SAR echo, including the geometric displacement, residual range migration and defocusing effect in both the range and azimuth dimensions, might be helpful to improve the performance of a SAR/GMTI&Im system. Many previous studies have investigated the effect of target motion on SAR image [8–10]. However, these discussions are mainly focused on the error analysis of phase history, which are equivalent to the analysis of target signatures on the SAR image obtained by 2-D separable SAR processing. To the authors' knowledge, until recently, little work is available in the literatures on the analysis of signatures of moving target after the application of fine resolution SAR processing. Thus the purpose of this paper is to develop the SAR image spectrum of moving target and give a detailed description of its signatures.

In the vast SAR literatures, a number of image formation algorithms [3] have been developed to form fine resolution images of the ground scene. From the perspective of data focusing adjustments, they can be divided into two classes: one is to operate in azimuth frequency domain, e.g., the range-Doppler algorithm (RDA), the chirp scaling algorithm (CSA) and the range migration algorithm (RMA); the other is to operate in the azimuth time domain, e.g., the polar format algorithm (PFA). Since the RDA and the CSA are both approximated implementations of RMA, the RMA and the PFA are chosen to show their responses to the moving target in this paper.

The organization of this paper is as follows. Section 2 defines the image-error-spectrum of moving target. In Section 3, the image-error-spectrum of moving target after the RMA and the PFA processing, respectively, are derived. Based on the formulation of image-error-spectrum in Section 3, Section 4 offers an insight into the SAR signatures of moving target. Finally, in Section 5, we give a simulation validation.

2. THE SAR IMAGE-ERROR-SPECTRUM MODEL OF MOVING TARGET

Consider a spotlight SAR operating with the geometry depicted by Fig. 1. For simplicity, we only examine the case in which the sensor travels along a straight line at constant forward velocity V_0, and suppose that the radar operates in the broadside mode. The central point of the illuminated scene is defined as the origin of the coordinate system, and the instantaneous position of radar antenna phase center

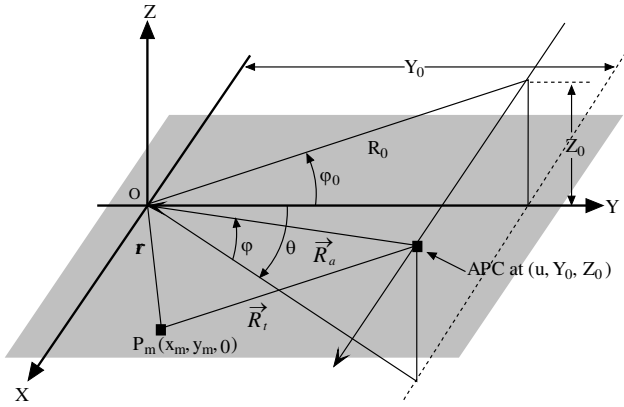

Figure 1. Spotlight SAR data collection geometry.

(APC) is denoted by the vector $\vec{R}_a = (u, Y_0, Z_0)$, where Y_0 and Z_0 keep constant in this geometry. Let t represent the slow time, then $u = V_0 t$ is the along track position on the OX axis. The variables θ and φ represent the APC's instantaneous squint angle and grazing angle, respectively, which equal θ_0 and φ_0, respectively, at the aperture center.

For a point target, after matched filtering, the demodulated baseband 2-D echo signal can be expressed as

$$S(u, f_\tau) = A \cdot \exp\left[-j\frac{4\pi(f_c + f_\tau)}{c} R_t(u)\right] \tag{1}$$

where A includes the nonessential factors of transmission pulse envelop and antenna pattern, c is the velocity of propagation, f_c is the radar carrier frequency (corresponding to wavelength λ), f_τ is the range frequency, and $R_t(u)$ is the instantaneous distance between the target and the APC.

2.1. General Description on Moving Target

Consider a point scatterer P_m moving at constant velocity (V_x, V_y) in the XY plane. Its instantaneous coordinates can be expressed as

$$\begin{aligned} x_m &= x_0 + V_x t = x_0 + v_x u \\ y_m &= y_0 + V_y t = y_0 + v_y u \end{aligned} \tag{2}$$

where (x_0, y_0) is position of the target at the time instant $t = 0$ (corresponding to the aperture center), and $(v_x, v_y) = (V_x/V_0, V_y/V_0)$ is the normalized velocity.

The instantaneous range from the radar to the moving target is identified via

$$R_t(u) = \sqrt{(u - x_m)^2 + (Y_0 - y_m)^2 + Z_0^2}. \quad (3)$$

By inserting (2) into (3), we obtain

$$R_t(u) = \sqrt{(mu - x_s)^2 + (Y_0 - y_s)^2 + Z_0^2} = \sqrt{(mu - x_s)^2 + R_s^2} \quad (4)$$

where

$$\begin{aligned} &m = \sqrt{(1-v_x)^2 + v_y^2}, \quad R_s = \sqrt{(Y_0 - y_s)^2 + Z_0^2} \\ &x_s = \frac{x_0(1-v_x) + (Y_0 - y_0)v_y}{m}, \quad y_s = Y_0 - \frac{-x_0 v_y + (Y_0 - y_0)(1-v_x)}{m} \end{aligned} \quad (5)$$

2.2. Image-Error-Spectrum Model of Moving Target

Assume that the stationary scene is described by a complex reflectivity $f(x, y)$, and the radar located at (u, Y_0, Z_0) in the spatial domain illuminates the target area with transmission signal $p(\tau)$. The radar radiation pattern is assumed to be omni-directional. The SAR echo signal can be expressed as

$$r(u, \tau) = \iint f(x, y)\, p\left(\tau - \frac{2\sqrt{(x-u)^2 + (y-Y_0)^2 + Z_0^2}}{c}\right) dxdy \quad (6)$$

where $2\sqrt{(x-u)^2 + (y-Y_0)^2 + Z_0^2}/c$ is the round-trip time delay from the radar to the target at position (x, y).

The SAR image formation process can be thought of as a linear transformation T, which maps the echo data into a complex image, attempting to recover the original scene complex reflectivity:

$$g(x, y) = T\{r(u, \tau)\} \approx f(x, y). \quad (7)$$

The 2-D Fourier transform of image $g(x, y)$ is referred to as *image-spectrum*

$$G(k_x, k_y) = \iint g(x, y) \exp(-jk_x x - jk_y y) dxdy. \quad (8)$$

For a single stationary point scatterer with unit reflectivity at position (x_0, y_0), the complex scattering density function is $f(x, y) = \delta(x - x_0, y - y_0)$. After SAR processing, its image spectrum is expected as

$$G_0(k_x, k_y) = \begin{cases} \exp(-jx_0 k_x - jy_0 k_y) & (k_x, k_y) \in \Omega \\ 0 & (k_x, k_y) \notin \Omega \end{cases} \quad (9)$$

where Ω is the support region of spatial frequency, or wavenumber domain.

For the moving target P_m, we use (9) to define the ideal image spectrum, which implies that the target is perfectly focused and located at (x_0, y_0). If the slant plane is selected as the image display plane (e.g., in the RMA), the corresponding coordinate of (x_0, y_0) is $(x_0, R_c - R_0)$ in the slant plane, therefore, the ideal image spectrum can be

$$G_0(k_x, k_y) = \begin{cases} \exp\left[-jx_0k_x - j\left(R_c - R_0\right)k_y\right] & (k_x, k_y) \in \Omega \\ 0 & (k_x, k_y) \notin \Omega \end{cases} \quad (10)$$

where k_y is the cross-track spatial frequency in slant plane, $R_c = \sqrt{(Y_0 - y_0)^2 + Z_0^2}$ is the cross-track range from the position (x_0, y_0) to radar, and $R_0 = \sqrt{Y_0^2 + Z_0^2}$ is the cross-track range from scene center to radar.

However, due to its motion, the moving target, after SAR image formation, almost always appears defocused and located at a false location in the image. In the spectrum domain, this fact can be described by a multiplicative error term that interferes with the ideal image spectrum

$$G_m(k_x, k_y) = G_0(k_x, k_y) \cdot G_\varepsilon(k_x, k_y). \quad (11)$$

In (11), the error term $G_\varepsilon(k_x, k_y)$ is referred to as *image-error-spectrum* of the moving target.

3. IMAGE-ERROR-SPECTRUM DERIVATION OF MOVING TARGET

In this section, the image-error-spectrum of moving target after the RMA and the PFA processing, respectively, are derived.

3.1. Image-Error-Spectrum of Moving Target for RMA

The first step of RMA is to take the along-track Fourier transform on the SAR signal history in (1) which is a chirp signal in azimuth. We show the signal history here again for clearness

$$S(u, k_r) = A \cdot \exp[-jk_rR_t(u)] = A \cdot \exp\left[-jk_r\sqrt{(mu - x_s)^2 + R_s^2}\right] \quad (12)$$

where $k_r = \frac{4\pi(f_c + f_\tau)}{c}$ is the spatial frequency corresponding to radial range, and m, x_s, R_s are defined in (5).

As is well known, there exists the following Fourier transform relationship in the derivation of RMA [3]

$$\exp\left[-jk_r\sqrt{(u - x_s)^2 + R_s^2}\right] \Leftrightarrow \exp\left[-j\left(x_sk_x + R_s\sqrt{k_r^2 - k_x^2}\right)\right]. \quad (13)$$

Using this Fourier transform pair and the scaling property of Fourier transform, we can get the along-track Fourier transform of (12)

$$S(k_x, k_r) = \bar{A} \cdot \exp\left\{-j\left[x_s \frac{k_x}{m} + R_s\sqrt{k_r^2 - \left(\frac{k_x}{m}\right)^2}\right]\right\}$$
$$= \bar{A} \cdot \exp\left\{-j\left[\frac{x_s}{m}k_x + R_s\sqrt{k_r^2 - k_x^2 + \varepsilon k_x^2}\right]\right\} \quad (14)$$

where $\varepsilon = 1 - \frac{1}{m^2}$, k_x is the along-track spatial frequency, and $\bar{A}$ is a complex constant.

The second step of RMA is the operation of matched filtering, where the transfer function contains the conjugate of all space-invariant phase terms [3]

$$S_{ref}(k_x, k_r) = \exp\left(jR_0\sqrt{k_r^2 - k_x^2}\right). \quad (15)$$

After application of the matched filter, the signal becomes

$$S_{mat}(k_x, k_r) = \bar{A} \cdot \exp\left[-j\left(\frac{x_s}{m}k_x + R_s\sqrt{k_r^2 - k_x^2 + \varepsilon k_x^2} - R_0\sqrt{k_r^2 - k_x^2}\right)\right]. \quad (16)$$

To get the image spectrum, the last step of RMA is the stolt interpolation, which performs the change of variable $\sqrt{k_r^2 - k_x^2} \to k_y$, where k_y is referred to as the across-track spatial frequency in the slant plane. Application of this transformation yields the image spectrum

$$G_m(k_x, k_y) = \bar{A} \cdot \exp\left[-j\left(\frac{x_s}{m}k_x + R_s\sqrt{k_y^2 + \varepsilon k_x^2} - R_0 k_y\right)\right]$$
$$\approx \bar{A} \cdot \exp\left\{-j\left[\frac{x_s}{m}k_x + (R_s - R_0)k_y + \frac{\varepsilon R_s}{2k_y}k_x^2\right]\right\} \quad (17)$$

Note that the image spectrum has the support region offset from zero. In the across-track spatial frequency, the offset is $k_{yc} = \frac{4\pi f_c}{c}$, which is independent on the target. However, in the along-track spatial frequency, the targets will have different support regions. In appendix A, we show that the support region is centered at $k_{xc} = \frac{4\pi m x_s}{\lambda\sqrt{x_s^2 + R_s^2}}$, and is bounded by $-\frac{\pi m^2 R_s^2 R_0}{\rho_a (x_s^2 + R_s^2)^{3/2}} \le k_x - k_{xc} \le \frac{\pi m^2 R_s^2 R_0}{\rho_a (x_s^2 + R_s^2)^{3/2}}$.

Consulting (10), (11) and (17), we can get the image-error-spectrum of moving target as

$$G_\varepsilon(k_x, k_y) = \bar{A} \cdot \exp\left\{-j\left[\left(\frac{x_s}{m} - x_0\right)k_x + (R_s - R_c)k_y + \frac{\varepsilon R_s}{2k_y}k_x^2\right]\right\} \quad (18)$$

When ignoring the high order terms, the two-dimensional Taylor series expansion of (18), centered about the location $(k_x, k_y) =$

(k_{xc}, k_{yc}), can be expressed as

$$G_\varepsilon(k_x,k_y)=\tilde{A}\cdot\exp\left\{-j\left[a_{10}(k_x-k_{xc})+a_{01}(k_y-k_{yc})+a_{20}(k_x-k_{xc})^2 +a_{11}(k_x-k_{xc})(k_y-k_{yc})+a_{02}(k_y-k_{yc})^2\right]\right\} \quad (19)$$

where

$$a_{10}=\frac{x_s}{m}-x_0+\frac{\varepsilon R_s k_{xc}}{k_{yc}}=x_s-x_0+\left(1-\frac{1}{m}\right)\left(\frac{(m+1)R_s}{\sqrt{x_s^2+R_s^2}}-1\right)x_s \quad (20a)$$

$$a_{01}=R_s-R_c-\frac{\varepsilon R_s k_{xc}^2}{2k_{yc}^2}=R_s-R_c-\frac{\left(m^2-1\right)x_s^2 R_s}{2\left(x_s^2+R_s^2\right)} \quad (20b)$$

$$a_{20}=\frac{\varepsilon R_s}{2k_{yc}}=\frac{\left(m^2-1\right)\lambda R_s}{8\pi m^2} \quad (20c)$$

$$a_{11}=-\frac{\varepsilon R_s k_{xc}}{k_{yc}^2}=-\frac{\left(m^2-1\right)\lambda x_s R_s}{4\pi m\sqrt{x_s^2+R_s^2}} \quad (20d)$$

$$a_{02}=0 \quad (20e)$$

In (20), the coefficients of linear phase terms determine target positioning error in the image, where a_{10} is related to azimuth positioning error and a_{01} to range positioning error; the quadratic coefficients determine the defocusing effect, where a_{20} is related to azimuth defocus, a_{02} to range defocus, and a_{11} to 2-D defocusing (also known as residual linear range walk).

3.2. Image-Error-Spectrum of Moving Target for PFA

For the PFA, the classic theory of radar imaging formulates it by indicating an intrinsic, but simple Fourier transform relationship between the complex reflectivity of the illuminated scene and the collected data (after motion compensation to scene center). PFA is composed of interpolation of the nominal polar samples onto a 2-D Cartesian raster and a 2-D FFT. In practice, the mostly adopted implementation of 2-D interpolation is the separable 1-D range and azimuth resampling. We should also mention that relative to the stationary scene, the moving target suffers even severer wavefront curvature effect. We will take this effect into account in the following derivation.

PFA operates on signal history with motion compensation to a fixed point, e.g., the scene center point. After such compensation, the echoed signal in (1) becomes

$$S(u,f_\tau)=A\cdot\exp\left[j\frac{4\pi(f_c+f_\tau)}{c}R_\Delta\right] \quad (21)$$

where $R_\Delta = R_a(u) - R_t(u)$ is referred to as the differential range [3].

The first step of PFA is to perform range resampling on this signal, which results in [14]

$$S_R(u, k_y) = A \cdot \exp\left(jk_y \frac{R_\Delta}{\cos\varphi\cos\theta}\right) \tag{22}$$

where $k_y = \frac{4\pi}{c}(f_c + f_\tau)\cos\varphi_0$ is the cross-track spatial frequency in the ground plane. Note that k_y is offset from zero, and is centered about $k_{yc} = \frac{4\pi}{c} f_c \cos\varphi_0$. In (22), both R_Δ and $\cos\varphi\cos\theta$ are functions of u. To perform the azimuth analysis, it is helpful to expand $\frac{R_\Delta}{\cos\varphi\cos\theta}$ into a series in u/Y_0. By using the Taylor expansion, and meanwhile ignoring the cubic and higher order terms, $\frac{R_\Delta}{\cos\varphi\cos\theta}$ can be expanded as

$$\frac{R_\Delta}{\cos\varphi\cos\theta} \approx y_0 + x_0\frac{u}{Y_0} + c_0 + c_1\frac{u}{Y_0} + c_2\left(\frac{u}{Y_0}\right)^2 \tag{23}$$

where $y_0 + x_0\frac{u}{Y_0}$ are the desired basic imaging terms for focusing the moving target, and $c_0 + c_1\frac{u}{Y_0} + c_2(\frac{u}{Y_0})^2$ are the undesired terms resulted from wavefront curvature and the motion of target. The coefficients can be expressed as

$$\begin{aligned}
c_0 &= \frac{-x_0^2 - y_0^2 + y_0^2\cos^2\varphi_0}{2Y_0} \\
c_1 &= -x_0 v_x - \left(y_0\sin^2\varphi_0 - Y_0\right)v_y + \frac{x_0 y_0\cos^2\varphi_0}{Y_0} \\
c_2 &= \frac{1}{2}\left\{-\left(m^2-1\right)Y_0 + \frac{\cos^2\varphi_0}{Y_0}\left[(x_0 + Y_0 v_y)^2 - y_0^2\cos^2\varphi_0 + 2Y_0 y_0 v_x\right]\right\}
\end{aligned} \tag{24}$$

which are derived in Appendix B.

With (23), the range-resampled signal in (22) becomes

$$S_R(u, k_y) = A \cdot \exp\left\{jk_y\left[y_0 + x_0\frac{u}{Y_0} + c_0 + c_1\frac{u}{Y_0} + c_2\left(\frac{u}{Y_0}\right)^2\right]\right\}. \tag{25}$$

The azimuth resampling is a range frequency dependent slow time rescaling procedure, which can also be interpreted as a keystone transform. The keystone transform is formulated as

$$S_A(u, k_y) = S_R\left(\frac{k_{yc}}{k_y}u, k_y\right) = S_R\left(\frac{f_c}{f_c + f_\tau}u, k_y\right) \tag{26}$$

which results in the image spectrum

$$G_m(k_x,k_y)=A\cdot\exp\left\{j\left(y_0k_y+x_0\frac{k_cu}{Y_0}+c_0k_y+c_1\frac{k_cu}{Y_0}+\frac{c_2}{k_y}\left(\frac{k_cu}{Y_0}\right)^2\right)\right\}$$
$$=A\cdot\exp\left\{j\left(y_0k_y+x_0k_x+c_0k_y+c_1k_x+\frac{c_2}{k_y}(k_x)^2\right)\right\} \quad (27)$$

where $k_x=\frac{k_cu}{Y_0}$ is the along-track spatial frequency. Unlike the cross-track spatial frequency, the along-track spatial frequency in (27) has an unbiased support region, i.e., its center $k_{xc}=0$, because the variable u is centered at zero. Meanwhile all the targets posses the same support region which is bounded with $|k_x|\le\pi/\rho_a$, where ρ_a is the along-track spatial resolution.

Using (9), (11) and (27), we obtain the image-error-spectrum

$$G_\varepsilon(k_x,k_y)=A\cdot\exp\left[j\left(c_0k_y+c_1k_x+\frac{c_2}{k_y}k_x^2\right)\right] \quad (28)$$

When ignoring the high order terms, the Taylor series expansion of (28) about in the vicinity of $(k_x,k_y)=(k_{xc},k_{yc})$ is

$$G_\varepsilon(k_x,k_y)=\widehat{A}\cdot\exp\left\{j\left[b_{10}(k_x-k_{xc})+b_{01}(k_y-k_{yc})+b_{20}(k_x-k_{xc})^2\right.\right.$$
$$\left.\left.+b_{11}(k_x-k_{xc})(k_y-k_{yc})+b_{02}(k_y-k_{yc})^2\right]\right\} \quad (29)$$

where

$$b_{10} = c_1=-x_0v_x-\left(y_0\sin^2\varphi_0-Y_0\right)v_y+\frac{x_0y_0\cos^2\varphi_0}{Y_0} \quad (30a)$$

$$b_{01} = c_0=\frac{-\left(x_0^2+y_0^2\right)+y_0^2\cos^2\varphi_0}{2Y_0} \quad (30b)$$

$$b_{20} = \frac{c_2}{k_{yc}}=\frac{1}{2k_{yc}}\left\{-\left(m^2-1\right)Y_0+\frac{\cos^2\varphi_0}{Y_0}\left[(x_0+Y_0v_y)^2\right.\right.$$
$$\left.\left.-y_0^2\cos^2\varphi_0+2Y_0y_0v_x\right]\right\} \quad (30c)$$

$$b_{11} = 0 \quad (30d)$$

$$b_{02} = 0 \quad (30e)$$

Corresponding to (20), the coefficients b_{10}, b_{01}, b_{20},b_{11} and b_{02} can be interpreted identically as a_{10},a_{01}, a_{20}, a_{11} and a_{02}, respectively. Also note that the phase error caused by plane wavefront approximation in PFA has been included in $G_\varepsilon(k_x,k_y)$.

4. SAR SIGNATURES OF MOVING TARGET

The SAR signatures of moving target can be derived from the target image-error-spectrum. Equations (19) and (29) represent the image-error-spectrum of moving target after RMA and PFA processing, respectively. As is stated in the previous section, the linear phase terms in the image-error-spectrum carry the phase information related to the displacement of moving target from the expected position; the quadratic terms in k_x and k_y cause defocus in azimuth and range, respectively; and the coupling terms of k_x and k_y, corresponds to the residual linear range migration.

4.1. Geometric Displacement of Moving Target

Moving target has no fixed position. However, after SAR processing, we hope that it locates at a specific position, which is referred to as nominal position in this paper, for example, the instantaneous position of target when the APC is at aperture center. Thus, after SAR processing, the difference between the actual geometrical position of moving target and this nominal position is defined in this paper as the *geometric displacement*. The coefficients of the linear phase terms in image-error-spectrum indicate these displacements.

The RMA is a precise image formation algorithm for stationary target, thus, the geometric displacement of moving target after RMA processing is determined only by the motion of target. From (1) and (4), we can see that the moving target with constant velocity has identical phase history with the particular stationary target located at $(x_s, R_s - R_0)$ in the slant plane but with a scaled sensor velocity mV_0 [15]. Using this equivalent sensor velocity mV_0, RMA can produce a focused image of the moving target but with an incorrect position of $(x_s, R_s - R_0)$ instead of the expected position $(x_0, R_c - R_0)$. Thus, the geometric displacement in azimuth and range are $\Delta x = x_s - x_0$ and $\Delta y = R_s - R_c$, respectively. However, SAR image formation, by design, aims to focus the stationary target. Sensor velocity used in the image formation procedure is the actual velocity V_0 rather than the equivalent velocity mV_0. Due to velocity mismatch, the moving target will appear to be defocused, and additional geometric displacement is introduced relative to $\Delta x = x_s - x_0$ and $\Delta y = R_s - R_c$. This can be seen from (20), where the coefficients of linear phase terms show that the actual geometric displacements in along-track and across-track

directions are

$$\Delta x = x_s - x_0 + \left(1 - \frac{1}{m}\right)\left(\frac{(m+1)\,R_s}{\sqrt{x_s^2 + R_s^2}} - 1\right)x_s \text{ and}$$

$$\Delta y = R_s - R_c - \frac{\left(m^2 - 1\right)x_s^2 R_s}{2\left(x_s^2 + R_s^2\right)}, \text{ respectively.}$$

As for the PFA, the geometric displacements result from not only the target's motion, but also the plane wavefront curvature effect. The azimuth displacement is determined by b_{10}, in which the term $x_0 y_0 \cos^2\varphi_0 / Y_0$ is due to the wavefront curvature effect, and the term $-x_0 v_x - (y_0 \sin^2\varphi_0 - Y_0)v_y$ is induced by the motion of target. It is clear that, besides the well-known Doppler shift effect $Y_0 v_y$ resulted from radial motion, along-track motion also causes azimuth displacement, although it is usually far less than $Y_0 v_y$. Displacement in range is determined by b_{01}. We can see in (30b) that, the range displacement is independent of the target's motion, and it equals that of the stationary target located at position (x_0, y_0) caused by wavefront curvature.

4.2. Residual Range Walk of Moving Target

For SAR image formation algorithms, the correction of range cell migration (RCM) is a key issue to be considered. One shortcoming of the conventional SAR approach, from the perspective of moving target imaging, lies in its image processing that, by design, focuses on the stationary target scene, while a moving target introduces additional range migration which the SAR image formation algorithms don't take into account. However, we will see from the following analysis that part of this additional migration can be naturally corrected during the SAR focusing process, although different image formation algorithms might have different capability for range migration correction. Consequently, the well-known limitation that the RCM of moving target during the coherent processing interval is expected not to exceed a fraction of a range resolution cell [8] can be alleviated, and only the residual range migration, which is much less than the original one, is limited not to exceed a fraction of a range resolution cell.

In the image-error-spectrum, the coupling terms of k_x and k_y are related to the residual range migration. When the relative bandwidth of transmitted signal is sufficiently small, the high order phase terms in the image-error-spectrum can be neglected. Therefore, the only residual range migration that we are concerned is the residual linear range walk.

For the RMA, the residual linear range walk of the moving target can be evaluated in the k_x-y plane, by inspecting the coupling phase term in (19):

$$\Delta R\left(k_x\right) = a_{11}\left(k_x - k_{xc}\right). \tag{31}$$

Therefore, after RMA processing, the total residual range walk during the coherent integration time is

$$\Delta R_{total} = a_{11}\Delta k_x = \frac{m\left(m^2-1\right)\lambda x_s R_0 R_s^3}{2\rho_a\left(x_s^2+R_s^2\right)^2} \tag{32}$$

where Δk_x is the width of support region in k_x which is derived in Appendix A. Thus, instead of the original range walk, only the above residual range walk is expected not to exceed a range resolution cell, i.e.,

$$\frac{m\left(m^2-1\right)\lambda x_s R_0 R_s^3}{2\rho_a\left(x_s^2+R_s^2\right)^2} \leq \rho_r \tag{33}$$

where ρ_r is the range resolution. As a special example, we consider the target in the scene center moving only in the OY direction ($v_x = 0$, $v_y \neq 0$), the range walk limitation can be simplified as a velocity limitation:

$$v_y \leq \sqrt[3]{\frac{2\rho_a\rho_r}{\lambda Y_0}} \quad \text{or} \quad V_y \leq V_0\sqrt[3]{\frac{2\rho_a\rho_r}{\lambda Y_0}}. \tag{34}$$

With the PFA, however, the result seems to be more favorable. We can see from (30d) that, the coefficient of the coupling term b_{11} is zero. It means that all the linear range walk of moving target is corrected, although no specific additional processing is employed. This phenomenon of linear range walk elimination can be also explained by considering the azimuth interpolation process of the PFA as the well-known keystone transform, which is originally used to correct unknown linear range migration of the moving target [11].

4.3. Focusing Property of Moving Target

Apart from the residual range migration, the quadratic phase terms are the main causes related to the defocusing effect. In the image-error-spectrums presented in (19) and (29), the quadratic terms are only related to k_x, which suggests that the defocusing effect occurs only in the along-track direction.

Similar to range walk, due to velocity mismatch, the moving target suffers residual quadratic phase error (QPE) $a_{20}k_x^2$ after the RMA

processing. Considering the support of along-track spatial frequency in RMA processing (Appendix A), the QPE can be calculated as

$$\Phi_{\mathrm{QPE}} = a_{20}\left(\frac{\Delta k_x}{2}\right)^2 = \frac{\pi m^2\left(m^2-1\right)\lambda R_0^2 R_s^5}{8\rho_a^2\left(x_s^2+R_s^2\right)^3}. \tag{35}$$

Neglecting its weak dependence on the target position, and setting the QPE allowance to be $\pi/2$, we can get the focusing limitation on the cross-track velocity

$$v_y \le 2\rho_a\sqrt{\frac{1}{\lambda R_0}}. \tag{36}$$

For the PFA, the residual quadratic phase error is $b_{20}k_x^2$. The maximum phase error evaluated at the edges of the azimuth spatial frequency support, is expressed as

$$\begin{aligned}\Phi_{\mathrm{QPE}} &= b_{20}\left(\frac{\Delta k_x}{2}\right)^2 = \frac{1}{2k_{yc}}\Big\{-\left(m^2-1\right)Y_0+\frac{\cos^2\varphi_0}{Y_0}\Big[\left(x_0+Y_0v_y\right)^2\\ &\quad -y_0^2\cos^2\varphi_0+2Y_0y_0v_x\Big]\Big\}\left(\frac{\pi}{\rho_a}\right)^2\\ &= \frac{1}{2k_{yc}}\left\{\left(2v_x-v_x^2-v_y^2\sin^2\varphi_0\right)Y_0+\frac{\cos^2\varphi_0}{Y_0}\left[x_0^2-y_0^2\cos^2\varphi_0\right.\right.\\ &\quad \left.\left.+2Y_0\left(y_0v_x+x_0v_y\right)\right]\right\}\left(\frac{\pi}{\rho_a}\right)^2\end{aligned} \tag{37}$$

which will be given an insight at below.

4.4. Further Discussion on the PFA

In the PFA processing, the residual quadratic phase error of moving target in (37) has a strong dependence on the target's position. Assuming that scene radius is r_0, we can infer that the right-hand side of (37) has an upper bound

$$\begin{aligned}\Phi_{\mathrm{QPE}}^{\max} &= \frac{\pi^2}{2\rho_a^2k_{yc}}\left\{\left(2\left|v_x\right|+v_x^2+v_y^2\sin^2\varphi_0\right)Y_0\right.\\ &\quad \left.+\frac{\cos^2\varphi_0}{Y_0}\left[r_0^2+2Y_0r_0\left(\left|v_x\right|+\left|v_y\right|\right)\right]\right\}.\end{aligned} \tag{38}$$

If the QPE allowance is set to be $\pi/2$, i.e., $\Phi_{\mathrm{QPE}}^{\max}\le\pi/2$, we have

$$\begin{aligned}&\frac{\pi^2}{2\rho_a^2k_{yc}}\left\{\left(2\left|v_x\right|+v_x^2+v_y^2\sin^2\varphi_0\right)Y_0\right.\\ &\left.+\frac{\cos^2\varphi_0}{Y_0}\left[r_0^2+2Y_0r_0\left(\left|v_x\right|+\left|v_y\right|\right)\right]\right\}\le\pi/2.\end{aligned} \tag{39}$$

Solving (39), we obtain an estimate for allowable scene radius r_0 of

$$r_0 \leq -\left(|v_x| + |v_y|\right) Y_0 + \frac{Y_0}{\cos\varphi_0}\sqrt{\frac{\rho_a^2 k_{yc}}{\pi Y_0}} + \left(|v_x| + |v_y|\right)^2 \cos^2\varphi_0 - \left(2\,|v_x| + v_x^2 + v_y^2 \sin^2\varphi_0\right) \quad (40)$$

for the moving target with normalized velocity v_x and v_y.

5. SIMULATION RESULTS

In this section, point target simulation is employed to validate the presented analysis. Parameters outlining the simulation are listed in Table 1. There are four point targets moving with constant velocity in the ground plane, whose motion parameters are illustrated in Fig. 2. The target's instantaneous position at aperture center is referred to as the nominal position, which is the reference when we discuss the geometric displacement. All the targets have different motion parameters, among which, target A, B, and D all traverse far more than one range resolution cell during the aperture time due to the radial motion.

The targets' signatures after the RMA and the PFA processing, respectively, are predicted using the above analysis and listed in Table 2. From the table, we can see that the residual range walk of target A, B, and C in both image formation algorithms are all less than a range resolution cell. Therefore, in the following discussion, target

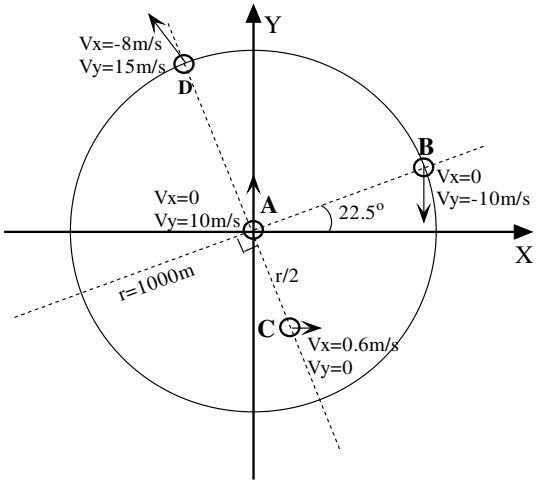

Figure 2. Arrangement of the simulated point targets.

A, B and C are chosen to validate the focusing property, while target D are selected to illustrate the difference between the PFA and the RMA in linear range migration correction. Moreover, the simulation results given at below will validate our prediction.

For each target, the 2-D impulse response function (IRF) after RMA and PFA processing, respectively, are presented in Fig. 3 and Fig. 4. In the following, we will give a detailed analysis on their signatures.

Table 3 gives the measured geometric displacement of moving target after SAR processing. It is clearly shown that the data determined by experiments are in good agreement with the theoretical results given in Table 2 within the range of measure errors. From the Table 3, we can also see that two image formation algorithms produce different geometric displacement. Moreover, besides the well-known azimuth Doppler shift effect, there also exist range positioning errors, which is often ignored in the existing literatures.

Table 1. Simulation parameters.

Parameter description	**Value**
Carrier frequency	10 GHz
Resolution (range × azimuth)	1 m × 1 m
Synthetic aperture time	4.5 s
Squint angle	0° (broadside)
Scene center range at aperture center	30000 m
Altitude	3000 m
Forward velocity of aircraft	100 m/s

Table 2. Theoretical signatures of moving target.

	Geometric Displacement (m, m)		**Residual Range Walk (m)**		**Quadratic Phase Error (rad)**	
	RMA	PFA	RMA	PFA	RMA	PFA
A	(2984.8, −148.9)	(2985.0, 0.0)	0.44	0.00	3.48	0.04
B	(−2946.6, −54.7)	(−2972.9, −14.3)	0.31	0.00	3.57	1.92
C	(−1.1, 0.0)	(−4.1, −0.7)	0.03	0.00	4.11	4.09
D	(4303.4, −262.9)	(4433.7, −2.6)	11.21	0.00	78.78	62.24

Table 3. Measured geometric displacement of moving target.

Geometric Displacement (m, m)	RMA	PFA
A	(2985.0, −149.3)	(2984.4, 0.0)
B	(−2946.9, −55.0)	(−2972.3, −14.6)
C	(−1.3, 0.2)	(−4.6, −0.6)
D	(4302.7, −262.6)	(4432.7, −2.7)

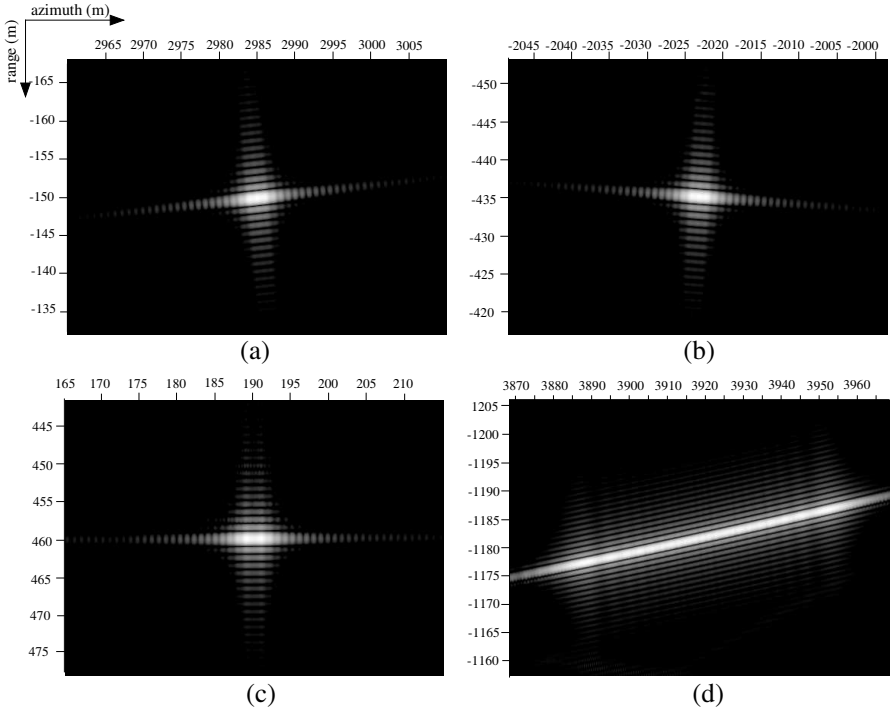

Figure 3. The 2-D IRF of moving target obtained using the RMA. (a) Target A, (b) target B, (c) target C, (d) target D.

From Fig. 3 and Fig. 4, we can clearly see that range migration of moving target has been partially corrected after image formation procedure, although no special attempt has been made to do this. Particularly, after PFA processing, the linear range migration, which is one of the dominant constraint on imaging of moving target, is completely eliminated.

From our analysis, we know that the motion of target only introduce azimuth defocus when the residual range migration can be neglected. Thus, in Fig. 5, we give the azimuth profile of the 2-D IRF of target A, B and C, which corresponding literally to the theoretical QPE in Table 2.

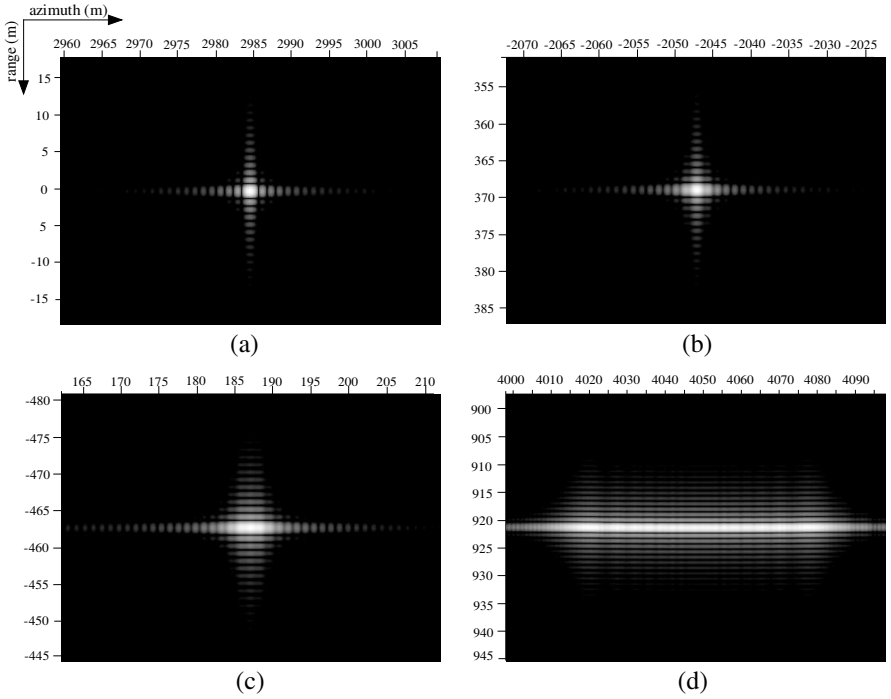

Figure 4. The 2-D IRF of moving target obtained using the PFA. (a) Target A, (b) target B, (c) target C, (d) target D.

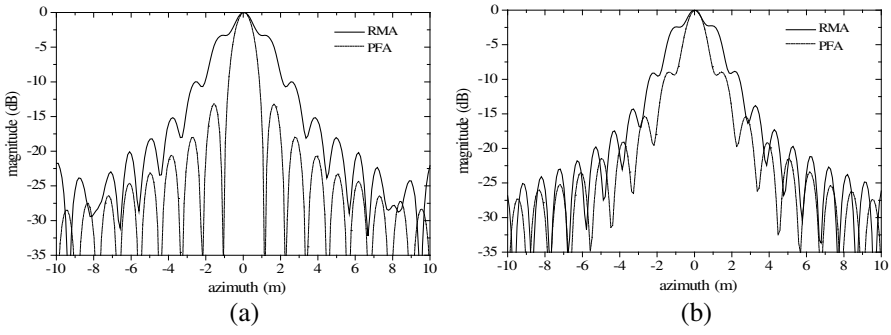

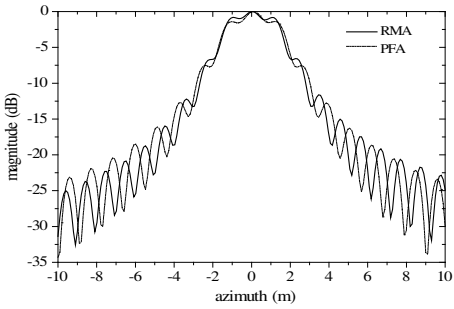

(c)

Figure 5. Azimuth profile of point target response. (a) Target A, (b) target B, (c) target C.

6. CONCLUSION

In this work, the image-error-spectrums of moving target after two representative high resolution SAR image formations processing, i.e., RMA and PFA, respectively, are derived. Based on these error spectrums, the SAR signatures of moving target, such as geometric displacement, residual range migration and defocus, which provide useful reference for the application in SAR/GMTI&Im, are presented.

In 2-D separable SAR processing, it is well-known that the SAR image of moving target with a component of velocity in the range direction appears shifted in azimuth only. However, we have demonstrated that the geometric displacement of moving target in high resolution SAR image lies essentially in two dimensions. That is to say, the target's motion also introduces range displacement.

After 2-D separable SAR processing, the additional range migration and phase error caused by target's motion are not treated at all. However, from our analysis, after high resolution SAR processing, the additional range migration and phase error can be partly corrected. Especially, after PFA processing, the linear range walk can be eliminated totally. Therefore, the well-known limitation on range migration for moving target [8] can be alleviated.

ACKNOWLEDGMENT

This work was supported in part by the Chinese Postdoctoral Science Foundation under Contract 20090461119, and 201003586, Jiangsu Planned Projects for Postdoctoral Research Funds under Contract 0902014C, Aeronautical Science Foundation of China under Contract 20102052024.

APPENDIX A.

In this appendix, we discuss the along-track spatial frequency support in RMA processing, i.e., the offset and the width of support region.

From (12), we know that the azimuth phase history of moving target can be expressed as

$$\varphi = -\frac{4\pi}{\lambda}\sqrt{(mu - x_s)^2 + R_s^2} \tag{A1}$$

It is an approximated LFM signal, whose center frequency is the first derivative of (A1) evaluated at the aperture center

$$k_{xc} = \frac{d\varphi}{du}\,|_{u=0} = \frac{4\pi m x_s}{\lambda\sqrt{x_s^2 + R_s^2}}, \tag{A2}$$

and the FM rate is the second derivative of (A1) evaluated at the aperture center

$$\dot{k}_{xc} = \frac{d^2\varphi}{du^2}\,|_{u=0} = \frac{4\pi m^2 R_s^2}{\lambda\left(x_s^2 + R_s^2\right)^{3/2}}. \tag{A3}$$

Accounting the synthetic aperture length $L = \lambda R_0/(2\rho_a)$, we can get the bandwidth of along-track spatial frequency

$$\Delta k_x = \dot{k}_{xc} L = \frac{2\pi m^2 R_s^2 R_0}{\rho_a\left(x_s^2 + R_s^2\right)^{3/2}}. \tag{A4}$$

APPENDIX B.

In this appendix, we derive the Taylor series expansion of $R_\Delta/(\cos\varphi\cos\theta)$ in (25).

For a target located at (x_m, y_m) on the XY plane in Fig. 1, the differential range is [3]

$$R_\Delta \approx \frac{\vec{R}_a \cdot \vec{r}_t}{R_a} - \frac{r_t^2}{2R_a} + \frac{\left(\vec{R}_a \cdot \vec{r}_t\right)^2}{2R_a^3} \tag{B1}$$

where

$$R_{basic} = \frac{\vec{R}_a \cdot \vec{r}_t}{R_a} = x_m \cos\varphi \sin\theta + y_m \cos\varphi\cos\theta \tag{B2}$$

is the basic imaging terms, and

$$\begin{aligned} R_{curve} &= -\frac{r_t^2}{2R_a} + \frac{\left(\vec{R}_a \cdot \vec{r}_t\right)^2}{2R_a^3} \\ &= \frac{-\left(x_m^2 + y_m^2\right) + \left(x_m\cos\varphi\sin\theta + y_m\cos\varphi\cos\theta\right)^2}{2R_a} \end{aligned} \tag{B3}$$

is the wavefront curvature terms.

For moving target, inserting the time-variant coordinates into (3), we can get

$$\frac{R_{basic}}{\cos\varphi\cos\theta}=x_m\tan\theta+y_m=y_0+(x_0+Y_0v_y)\left(\frac{u}{Y_0}\right)+Y_0v_x\left(\frac{u}{Y_0}\right)^2 \quad \text{(B4)}$$

$$\begin{aligned}\frac{R_{curve}}{\cos\varphi\cos\theta} &= \frac{-\left[(x_0+v_xu)^2+(y_0+v_yu)^2\right]}{2Y_0} \\ &+\frac{\cos^2\varphi\cos^2\theta\left[(x_0+v_xu)\frac{u}{Y_0}+(y_0+v_yu)\right]^2}{2Y_0}. \quad \text{(B5)}\end{aligned}$$

In (B5), the variable φ and θ are still function of u. To facilitate the Taylor series expansion, it is necessary to have expression $\cos^2\varphi\cos^2\theta$ in terms of u. Accounting the imaging geometry, the following relationship existed

$$\cos^2\varphi\cos^2\theta=\frac{1}{1+\tan^2\varphi_0+\tan^2\theta}=\frac{1}{1+\tan^2\varphi_0+u^2/Y_0^2}. \quad \text{(B6)}$$

Inserting (B6) into (B5), then perform the Taylor series expansion, we can get

$$\begin{aligned}\frac{R_{curve}}{\cos\varphi\cos\theta}=&\frac{-\left(x_0^2+y_0^2\right)+y_0^2\cos^2\varphi_0}{2Y_0}+[-x_0v_x-y_0v_y \\ &+(x_0+Y_0v_y)\,y_0\cos^2\varphi_0/Y_0]\frac{u}{Y_0}+\frac{1}{2}\left\{-\left(v_x^2+v_y^2\right)Y_0\right. \\ &\left.+\cos^2\varphi_0\left[(x_0+Y_0v_y)^2-y_0^2\cos^2\varphi_0+2Y_0y_0v_x\right]/Y_0\right\}\left(\frac{u}{Y_0}\right)^2 \quad \text{(B7)}\end{aligned}$$

where cubic and higher order terms are ignored.

Combined (B4) and (B7), the Taylor series expansion of $R_\Delta/(\cos\varphi\cos\theta)$ can be expressed as

$$\frac{R_\Delta}{\cos\varphi\cos\theta}=y_0+x_0\frac{u}{Y_0}+c_0+c_1\frac{u}{Y_0}+c_2\left(\frac{u}{Y_0}\right)^2 \quad \text{(B8)}$$

where

$$\begin{aligned}c_0&=\frac{1}{2}\left(-x_0^2-y_0^2+y_0^2\cos^2\varphi_0\right)/Y_0 \\ c_1&=-x_0v_x-\left(y_0\sin^2\varphi_0-Y_0\right)v_y+x_0y_0\cos^2\varphi_0/Y_0 \\ c_2&=\frac{1}{2}\left\{-\left(m^2-1\right)Y_0+\cos^2\varphi_0\left[(x_0+Y_0v_y)^2-y_0^2\cos^2\varphi_0\right.\right. \\ &\left.\left.+2Y_0y_0v_x\right]/Y_0\right\}. \quad \text{(B9)}\end{aligned}$$

REFERENCES

1. Kong, J. A., S. H. Yueh, H. H. Lim, R. T. Shin, and J. J. van Zyl, "Classification of earth terrain using polarimetric synthetic aperture radar images," *Progress In Electromagnetics Research*, Vol. 3, 327–370, 1990.
2. Lim, K.-S. and V. C. Koo, "Design and construction of wideband vna ground-based radar system with real and synthetic aperture measurement capabilities," *Progress In Electromagnetics Research*, Vol. 86, 259–275, 2008.
3. Carrara, W. G., R. S. Goodman, and R. M. Majewski, *Spotlight Synthetic Aperture Radar: Signal Processing Algorithms*, Artech House, Norwood, MA, 1995.
4. Chan, Y. K. and V. C. Koo, "An introduction to synthetic aperture radar (SAR)," *Progress In Electromagnetics Research B*, Vol. 2, 27–60, 2008.
5. Sabry, R. and P. W. Vachon, "Advanced polarimetric synthetic aperture radar (SAR) and electro-optical (eo) data fusion through unified coherent formulation of the scattered EM field," *Progress In Electromagnetics Research*, Vol. 84, 189–203, 2008.
6. Lim, K.-S. and V. C. Koo, "Design and construction of wideband vna ground-based radar system with real and synthetic aperture measurement capabilities," *Progress In Electromagnetics Research*, Vol. 86, 259–275, 2008.
7. Zheng, W., Z. Zhao, and Z.-P. Nie, "Application of TRM in the UWB through wall radar," *Progress In Electromagnetics Research*, Vol. 87, 279–296, 2008.
8. Raney, R. K., "Synthetic aperture imaging radar and moving targets," *IEEE Trans. Aerosp. Electron. Syst.*, Vol. 7, No. 3, 499–505, 1971.
9. Freeman, A. and A. Currie, "Synthetic aperture radar (SAR) images of moving targets," *GEC J. Res.*, Vol. 5, No. 2, 106–115, 1987.
10. Chen, V. C., "Radar imaging of ground moving targets," *Proc. IEEE Radar Conf.*, 426–431, Atlanta, GA, 2001.
11. Perry, R. P., R. C. Dipietro, and R. L. Fante, "SAR imaging of moving targets," *IEEE Trans. Aerosp. Electron. Syst.*, Vol. 35, No. 1, 188–200, 1999.
12. Choi, G. G., S. H. Park, H. T. Kim, and K. T. Kim, "ISAR imaging of multiple targets based on particle swarm optimization and hough transform," *Journal of Electromagnetic Waves and Applications*, Vol. 23, No. 14–15, 1825–1834, 2009.

13. Bimpas, M., N. Paraskevopoulos, K. Nikellis, D. Economou, and N. K. Uzunoglu, "Development of a three band radar system for detecing trapped alive humans under building ruins," *Progress In Electromagnetics Research*, Vol. 49, 161–188, 2004.
14. Doerry, A. W., "SAR processing with stepped chirps and phased array antennas," *Sandia National Laboratories*, Albuquerque, New Mexico, 2006.
15. Minardi, M. J. and E. G. Zelnio, "Comparison of SAR based GMTI and standard GMTI in a dense target environment," *Proc. SPIE*, 2006.